Chemical Science

ROYAL SOCIETY OF CHEMISTRY

EDGE ARTICLE

View Article Online
View Journal

Cite this: DOI: 10.1039/d5sc10222g

All publication charges for this article have been paid for by the Royal Society of Chemistry

Bridging-patching *c*-pores with tetrafluorosuccinate in a *csq*-type mesoporous Zr-MOF with different crystal dimensions: cycling stability and adsorption kinetics for in-door humidity control

Hao Lin,[a] Huiying Lin,[a] Mingxing Zhang,[c] Yingpeng Jiang,[a] Yuhang Liu,[a] Liting Du[b] and Zhiyong Lu *[a]

Received 31st December 2025
Accepted 3rd May 2026

DOI: 10.1039/d5sc10222g

rsc.li/chemical-science

Metal–organic frameworks (MOFs) are promising for energy-efficient indoor humidity control, yet their long-term cycling stability is crucial. While Zr-MOFs featuring specific structural parameters—one-dimensional channels with neighbouring coplanar Zr_6 clusters spaced below 5.4 Å—typically demonstrate high hydrolytic stability due to restricted water accessibility, exceptions exist. The framework NU-1008, although meeting these criteria, shows sub-optimal cycling stability due to hydrolysis of its *c*-pore formate ligands, which compromises structural integrity. To address this, a Solvent Assisted Ligand Incorporation (SALI) strategy is employed to install auxiliary ligands within its *c*-pore. Modification with tetrafluorosuccinate (TFS) yields NU-1008-TFS, which exhibits exceptional stability, retaining 97.7% of its initial water uptake after four cycles and 99.4% of its original surface area. The derived bulk single-crystal material, NU-1008-SC-TFS, integrates this high stability with a substantial water capacity (0.80 g g^{-1}) and rapid kinetics (0.34 mg g^{-1} s^{-1}), positioning it as a promising candidate adsorbent for an intelligent humidity management system.

Introduction

Benefiting from the fast development of human society, increasing attention is being directed toward creating comfortable living and working environments, such as indoor humidity and air quality control.[1,2] Maintaining optimal indoor humidity levels (45–65% RH) is critical for both human well-being and building integrity. Excessive moisture promotes mold growth, damages structures, and impairs thermal comfort by hindering evaporative heat dissipation, while inadequate humidity compromises respiratory health.[3–5] Conventional humidity control relies on energy-intensive hybrid systems (*e.g.*, desiccant dehumidifiers coupled with vapor compression cooling), which decouple latent and sensible loads but incur high operational costs—especially in hot, humid climates with high latent loads. Passive alternatives like hygroscopic cloth curtains offer limited moisture buffering but suffer from low water uptake capacity and slow kinetics, restricting their effectiveness to moderate climates and often requiring intermittent operation.[6–8]

Metal–organic frameworks (MOFs) have emerged as a transformative solution for intelligent humidity management.[9–32] Their exceptional properties – including ultrahigh water adsorption capacity (*e.g.*, MIL-101-Cr's S-shaped isotherms), rapid sorption kinetics, and low regeneration temperatures (<60 °C) enable continuous, energy-efficient moisture control.[33,34] Unlike traditional materials, MOFs can be integrated into building systems (*e.g.*, ventilated façades) to actively "pump" indoor moisture outdoors *via* vapor pressure gradients, independently of outdoor humidity conditions. This eliminates the need for energy-intensive air dilution and reduces sensible cooling loads by up to 86% compared to conventional systems. Moreover, their tunable structures allow precise humidity regulation, making MOFs pivotal for next-generation sustainable buildings in humid regions.[35–38]

For adsorption-based intelligent humidity management, the performance of adsorbents is the key factor that determines the efficiency. Basically, structural stability and adsorption efficiency (including capability and kinetics) are two critical requirements for adsorbents used in these water adsorption applications.[34,39,40] Materials must endure repeated adsorption–desorption cycles; poor cycling stability leads to gradual degradation or complete loss of adsorption capacity, severely

[a]College of Chemistry and Molecular Engineering, Nanjing Tech University, Nanjing 210009, China. E-mail: zhiyong.lu@njtech.edu.cn
[b]Advanced Analysis and Testing Center, Nanjing Forestry University, Nanjing 210037, China
[c]College of Chemistry and Chemical Engineering, Nantong University, Nantong 226019, China

compromising performance. Our previous studies identified that Zr-MOFs featuring one-dimensional channels, with coplanar adjacent Zr_6 clusters aligned along the channel direction, and a cluster spacing below 5.4 Å exhibit not only excellent hydrolytic stability but also enhanced structural stability.[41] This arises from limited water molecule accessibility to Zr_6 nodes solely along the one-dimensional channel direction, resulting in superior water adsorption cycling stability. However, during our research, we noticed that even certain Zr-MOFs meeting these structural criteria displayed cycling stability below expectations, such as NU-1008 constructed from Zr_6 nodes and TCPB-Br_2^{4-} linkers.[41,42] We attributed this to the disorder and gradual hydrolysis of formate ligands between adjacent coplanar Zr_6 clusters along the channel direction in NU-1008 (*c*-pore area). The departure of these formate ligands in the *c*-pore area allows water molecules to penetrate between clusters. The resulting unbalanced capillary forces during water extraction can induce localized structural collapse, leading to a slight decline in cycling stability.

To address this, in this contribution, we employed the Solvent Assisted Ligand Incorporation (SALI)[43–45] method to introduce auxiliary ligands with a smaller pK_a value than formic acid in the *c*-pore area of NU-1008 for further strengthening the coordination interaction around the *c*-pore, aiming to prolong the restriction of node accessibility and thereafter enhance cycling stability. Among the auxiliary-ligand-functionalized NU-1008 analogues, the introduction of bitopic coordinating tetrafluorosuccinic acid shows the most optimized water adsorption cycling stability of NU-1008. The resultant material NU-1008-TFS retained 97.7% of its initial water uptake capacity by the fourth cycle, and its BET surface area after water adsorption cycles remained at 99.4% of the value before the water adsorption test, demonstrating exceptional stability. Further investigation into its adsorption kinetics revealed its close correlations with particle-size-induced packing density instead of the length/diameter ratio. The ultimate bulk single crystal sample NU-1008-SC-TFS combines high stability, high water-vapor uptake capacity (0.80 g g^{-1}) as well as fast kinetics (0.34 mg g^{-1} s^{-1}), making it a promising candidate for adsorption-based intelligent indoor humidity control.

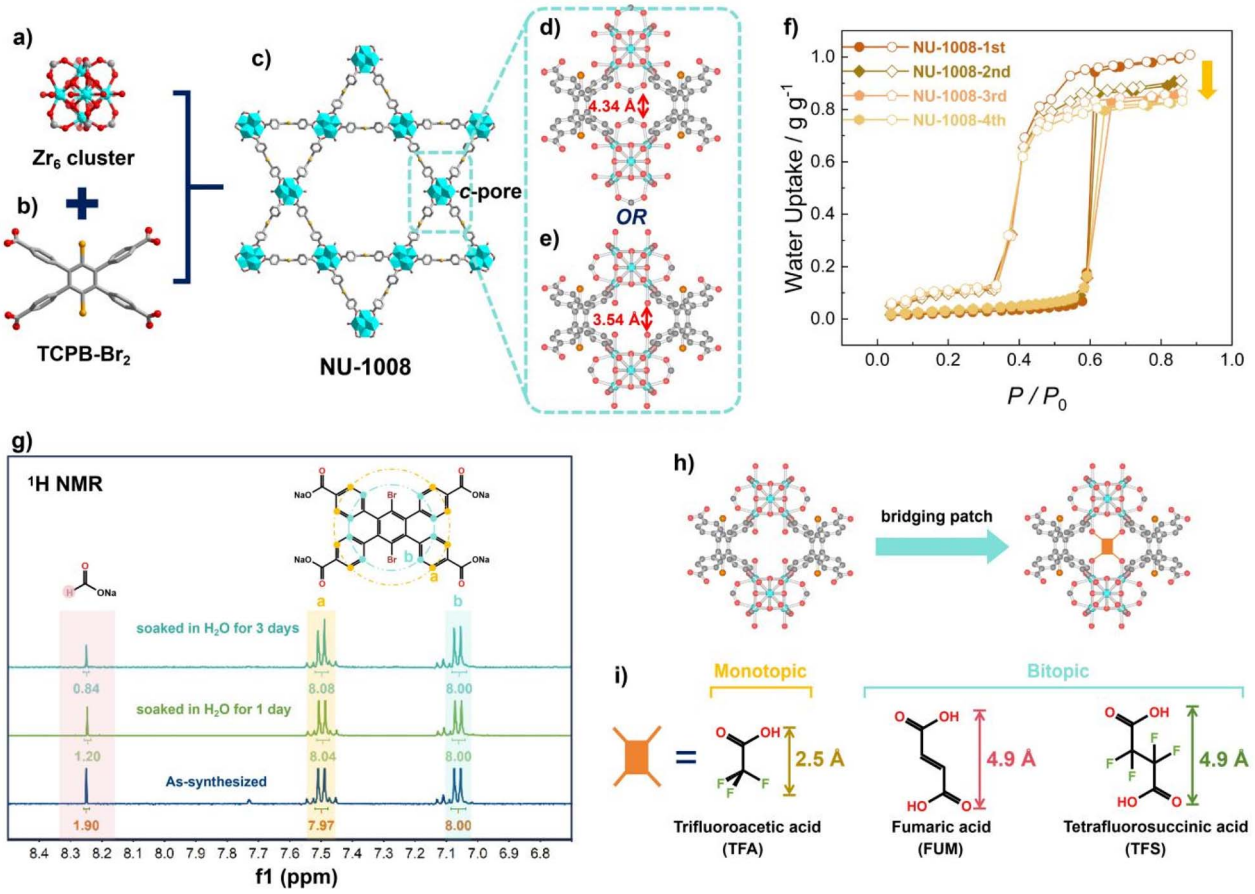

Fig. 1 Schematic depiction of structural degradation and complementary modification of the *c*-pore region in NU-1008. (a) The Zr_6 cluster; (b) the TCPB-Br_2^{4-} linker; (c) the typical *csq*-type network of NU-1008; (d) the *c*-pore environment in NU-1008 with formate coordinated inside the pore; (e) the *c*-pore environment in NU-1008 with formate coordinated toward the mesopore; (f) water-vapor adsorption isotherms of NU-1008 over four consecutive cycles; (g) ^{1}H NMR spectra of the base-digested NU-1008 sample after prolonged soaking in water (replaced every 8 h), showing the gradual decrease in formate content; (h) illustration of *c*-pore patching *via* bridging linkers; (i) chemical structures of the selected candidate linkers for *c*-pore patching: monotopic TFA, bitopic FUM, and bitopic TFS.

Table 1 Comparison of water-vapor cycling stability of NU-1008 analogues

MOFs	Auxiliary ligand content ($L:Zr_6$)	Saturated N_2 uptake ($cm^3\ g^{-1}$)	BET ($m^2\ g^{-1}$)	N_2 uptake after 4 cycles ($cm^3\ g^{-1}$)	BET after 4 cycles ($m^2\ g^{-1}$)	BET loss (%)	Water capacity for the 1st cycle ($g\ g^{-1}$)	Water capacity for the 4th cycle ($g\ g^{-1}$)	Water capacity loss (%)
NU-1008	—	609.9	1482.1	491.7	1315.6	11.2	1.00	0.83	17.0
NU-1008-FUM	0.73 : 1	722.9	1708.3	618.9	1442.5	15.6	0.90	0.88	2.2
NU-1008-TFA	3.89 : 1	590.7	1279.7	543.3	1230.0	3.9	0.81	0.76	6.2
NU-1008-TFS	0.74 : 1	644.2	1400.8	616.9	1392.2	0.6	0.87	0.85	2.3

Results and discussion

Degradation of NU-1008 during water adsorption

NU-1008 is a *csq*-topology Zr-based metal–organic framework synthesized from Zr(IV) and the tetratopic linker TCPB-Br_2^{4-}, featuring hierarchical porosity with two distinct channel types: micropores (~1 nm in diameter) and mesopores (~3 nm in size) (Fig. 1a–c).[46] Each Zr_6 node possesses 12 potential coordination sites, eight of which are occupied by TCPB-Br_2^{4-} linkers, while the remaining sites are coordinated with non-structural species such as aqua, hydroxyl groups, or modulator molecules. Along the channel direction, the distance between adjacent coplanar Zr_6 nodes measures 4.3 Å (Fig. 1d), satisfying the geometric criteria previously proposed for achieving high water-adsorption cycling stability in Zr-MOFs.[41] Despite this, NU-1008 still exhibits a gradual decline in water uptake over repeated cycles (Fig. 1f and Table 1), with the fourth-cycle saturation capacity dropping to approximately 83% of the initial value. Correspondingly, the BET surface area derived from N_2 adsorption shows an 11.2% reduction after four water-vapor adsorption cycles. This behavior contrasts with other Zr-MOFs that fully meet the stability requirements outlined in our earlier work.[41]

To clarify the structural details of NU-1008, we re-examined its single-crystal structure. Unlike previously reported,[46] formate ligands were clearly resolved at sites directed toward the mesopores (Fig. 1e), whereas none were observed around the *c*-pore region (Fig. 1d). However, ^{1}H NMR analysis of the digested as-synthesized sample indicates approximately four formate ligands per Zr_6 node (Fig. 1g), implying that nearly two formates are located near the *c*-pore but are highly disordered and thus not discernible in the electron density map. Moreover, coordinated formate ligands are susceptible to hydrolysis under prolonged exposure to aqueous environments (Fig. 1g). Collectively, disorder and potential hydrolysis of formates around the *c*-pore can create local defects, allowing water penetration and inducing imbalanced capillary stresses. These factors are together responsible for the progressive degradation observed during repeated water-vapor adsorption cycles.

Solvent Assisted Ligand Incorporation (SALI) in NU-1008

To address the potential instability of formate ligands within the *c*-pore region, we proposed to further strengthen the connectivity along the *c*-axis in NU-1008, thereby achieving a more durable seal of the *c*-pores. Several auxiliary ligands with pK_a values lower than that of formic acid (pK_a = 3.75) were selected for coordination within the *c*-pore area. These included the monotopic trifluoroacetic acid (TFA, pK_a = 0.25) and the bitopic fumaric acid (FUM, pK_{a1} = 2.86)[47] and tetrafluorosuccinic acid (TFS, pK_{a1} = −1.03), as shown in Fig. 1i. TFA has previously been employed to enhance the water-vapor cycling stability of Zr-MOFs by acting as a protective ligand that shields the Zr_6 nodes from hydrolysis.[15,48] However, as a monotopic ligand, its coordination saturates all the available open sites in NU-1008, which precludes any subsequent application requiring accessible Lewis acid sites. In contrast, bitopic ligands can be installed in a bridging coordination mode

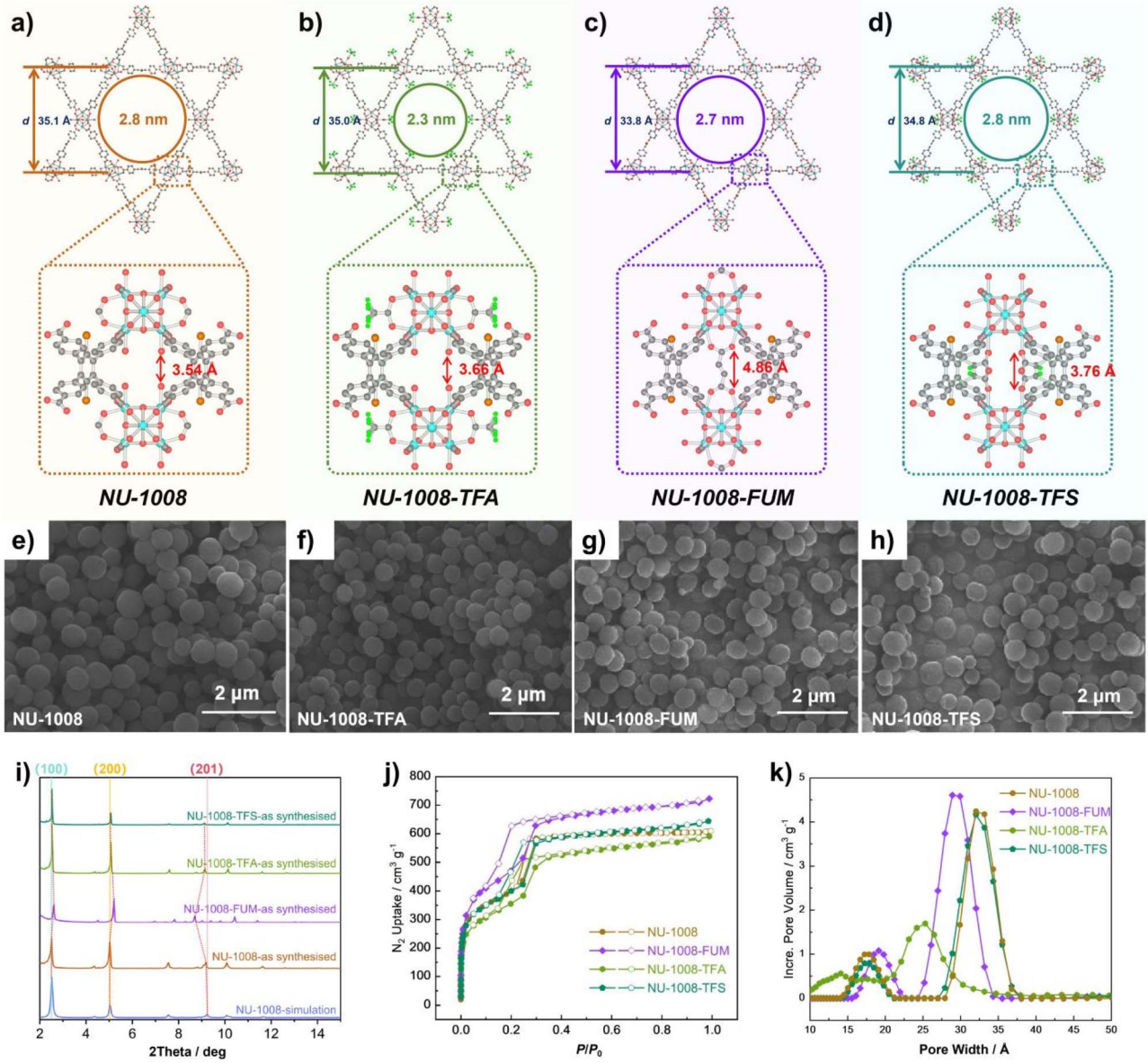

Fig. 2 Structural and physical characterization of NU-1008 and its analogues. (a–d) Crystal structures of pristine NU-1008 (a), NU-1008-TFA (b), NU-1008-FUM (c), and NU-1008-TFS (d); (e–h) corresponding scanning electron microscopy (SEM) images; (i) powder X-ray diffraction (PXRD) patterns; (j) N_2 adsorption–desorption isotherms measured at 77 K; (k) pore size distribution profiles derived from the adsorption data.

directly within the *c*-pore (Fig. 1h). This configuration effectively patches the pore while preserving the unsaturated metal sites directed toward the mesopore, leaving them accessible for further functionalization.

The SALI (solvent-assisted ligand incorporation) procedure was conducted following established protocols.[43,44,49] With the exception of TFA-loaded NU-1008, all samples containing bitopic ligands were subsequently treated with HCl/DMF at 120 °C to remove any mono-coordinated species. As characterized by ^{1}H NMR and summarized in Table 1, the ligand loadings per Zr_6 node for TFA, FUM, and TFS are 3.89, 0.73, and 0.74, respectively, aligning closely with theoretical expectations. Single-crystal structures were further determined for each sample. In NU-1008-TFA (Fig. 2b), the unsaturated metal sites facing the mesopores were confirmed to be occupied by TFA ligands. Although high disorder prevented the resolution of individual TFA molecules within the *c*-pore, the ^{1}H NMR-derived loading (Fig. S18 and Table 1) indicates the presence of two independent TFA molecules per pore. The distance between the coordinating oxygen atoms remained unchanged from that of pristine NU-1008. For NU-1008-FUM, bridging fumarate ligands were clearly identified within the *c*-pore, chelating to adjacent Zr_6 nodes on both sides (Fig. 2c). The extended length of this ligand increased the distance between coordinating oxygen atoms to 4.9 Å. TFS, while similar in size to fumarate, adopts a cisoid conformation. This results in a distinct mono-coordinated, bridging mode between neighboring Zr_6 nodes (Fig. 2d).

The conformation closely matches the pristine *c*-pore dimensions, causing only a minor expansion (3.76 Å *vs.* 3.54 Å).

Notably, the *c*-pore expansion in these analogues corresponds to a systematic decrease in the *d*-spacing of the (100) crystallographic plane (Fig. 2 and 1a–d). The values for NU-1008-TFA, NU-1008-FUM, and NU-1008-TFS are 35.0 Å, 33.8 Å, and 34.8 Å, respectively, compared to 35.1 Å for NU-1008. This change directly influences the mesopore dimensions. By accounting for van der Waals radii, the mesopore sizes were estimated from the crystal structures. Consistent with the reduced *d*-spacing, NU-1008-FUM shows a slight contraction (2.7 nm *vs.* 2.8 nm for NU-1008), while NU-1008-TFS retains a mesopore size comparable to the parent framework. Due to direct coordination within the mesopore, NU-1008-TFA exhibits the most significant pore size reduction. From the standpoint of preserving porosity, the terminal ligand TFA is therefore a suboptimal choice compared to bitopic linkers.

Upon scaling up the synthesis of NU-1008 analogues for adsorption testing, the phase purity of each sample was further verified by SEM and PXRD. Using the same batch of pristine NU-1008 as the starting material, all samples retained their original morphology following the SALI process, as shown in Fig. 2e–h. The PXRD patterns of the as-synthesized powder samples correspond well with those simulated from their respective single-crystal structures (Fig. S6, S11, S17 and S23). Due to the different connectivities introduced by the auxiliary ligands within the *c*-pore region, corresponding shifts in their PXRD patterns are observed. Compared to pristine NU-1008, all SALI analogues exhibit an expansion of the *c*-pore in their crystal structures, which is consistent with a shift of the (201) diffraction peak toward lower angles (Fig. 2i). The peak positions are as follows: NU-1008 at 9.18° (corresponding to a *c*-pore size of 3.54 Å in the single-crystal structure), NU-1008-FUM at 8.71° (4.86 Å), NU-1008-TFA at 9.13° (3.66 Å), and NU-1008-TFS at 9.11° (3.76 Å). Notably, the substantial expansion of the *c*-pore in NU-1008-FUM is accompanied by a modest contraction of the mesopore. As indicated in Fig. 2i, the (100) diffraction peak for NU-1008-FUM appears at 2.61°, shifted to a higher angle relative to that of NU-1008 at 2.51°. This corresponds to a decreased *d*-spacing of the mesopore, measured as 33.8 Å for NU-1008-FUM. In contrast, NU-1008-TFA and NU-1008-TFS exhibit their (100) diffraction peaks at 2.53° and 2.53°, respectively, indicating a slight shift toward lower angles compared to the pristine material.

Porosity characterization for NU-1008 analogues

The porosity of NU-1008 analogues was further characterized by N_2 adsorption at 77 K. As illustrated in Fig. 2j, compared with pristine NU-1008, the incorporation of different auxiliary ligands leads to distinct N_2 adsorption behaviors. NU-1008-TFS exhibits an adsorption isotherm similar to that of NU-1008, whereas NU-1008-TFA shows a moderate reduction in N_2 saturation capacity. Among the series, only NU-1008-FUM displays an enhanced N_2 adsorption isotherm, with a BET surface area of 1708.3 $m^2\ g^{-1}$, significantly higher than that of pristine NU-1008 (1482.1 $m^2\ g^{-1}$). The decreased N_2 adsorption isotherms of NU-1008-TFA and NU-1008-TFS correspond to reduced BET surface areas of 1279.7 $m^2\ g^{-1}$ and 1400.8 $m^2\ g^{-1}$, respectively (Table 1). Notably, compared with pristine NU-1008, all the modified analogues show pronounced hysteresis, which is caused by the increased complexity of the pore environment after auxiliary ligand incorporation. Such complexity confines N_2 molecules around the *c*-pore area and contributes to the great resistance of N_2 molecules during the desorption process. According to the pore size distribution (Fig. 2k), NU-1008-FUM exhibits an increase in micropore width (19 Å) and a decrease in mesopore width (29 Å), compared with NU-1008 (micropore: 17.3 Å; mesopore: 32.1 Å). Despite these alterations, the overall pore volume increase in NU-1008-FUM—reflected in its elevated N_2 adsorption—can be attributed to the expansion of the *c*-pore distance along the *c*-axis. For NU-1008-TFA, coordination of TFA within the mesopore region narrows the mesopore to approximately 25.3 Å, accompanied by a decrease in pore volume. In the case of NU-1008-TFS, aside from a slight reduction in pore volume, no significant pore contraction is observed. Although minor discrepancies exist between the pore sizes derived from N_2 adsorption and those obtained from crystallographic measurements, the variations in pore size distribution across the NU-1008 analogues remain consistent with the structural modifications observed in their crystal architectures.

Water-vapor adsorption and the cycling stability test

To evaluate the influence of auxiliary ligands on water adsorption capacity and cycling stability, water adsorption isotherms at 298 K were measured for the NU-1008 analogues (Fig. 3a). Following the incorporation of the auxiliary ligands, the characteristic inflection points of the isotherms shifted slightly toward higher relative humidity, which can be attributed to the enhanced hydrophobicity imparted by these ligands. Regarding water uptake capacity, all analogues exhibited a modest reduction compared to pristine NU-1008 (1.00 $g\ g^{-1}$), with saturated adsorption capacities of 0.81, 0.87, and 0.90 $g\ g^{-1}$ for NU-1008-TFA, NU-1008-TFS, and NU-1008-FUM, respectively. NU-1008-TFA, whose mesopores are notably narrowed by TFA ligands, demonstrated the lowest saturation uptake among the series.

The cycling stability of these materials was further investigated (Fig. 3b–d). Pristine NU-1008 exhibited a gradual degradation with each cycle, incurring a 17.0% loss in water adsorption capacity after four cycles (Fig. 3e), resulting in a fourth-cycle saturation uptake of 0.83 $g\ g^{-1}$. Functionalization with hydrophobic auxiliary ligands around the Zr_6 nodes markedly improved cycling stability. In NU-1008-TFA, the high local fluorine concentration around the nodes creates a hydrophobic microenvironment that impedes water access, leading to significantly enhanced stability relative to the parent framework. This material showed only a 6.2% capacity loss after four cycles (Fig. 3e), retaining an uptake of 0.76 $g\ g^{-1}$ in the fourth cycle (Fig. 3c and Table 1). For NU-1008-FUM, the fumarate (FUM) linker bridges adjacent Zr_6 clusters along the *c*-pore, serving both as a structural patch sealing the *c*-pore and a pillar that reinforces the framework against compressive or tensile forces along the *c*-axis. This bridging effect contributes to exceptional cycling stability, with a minimal capacity decrease

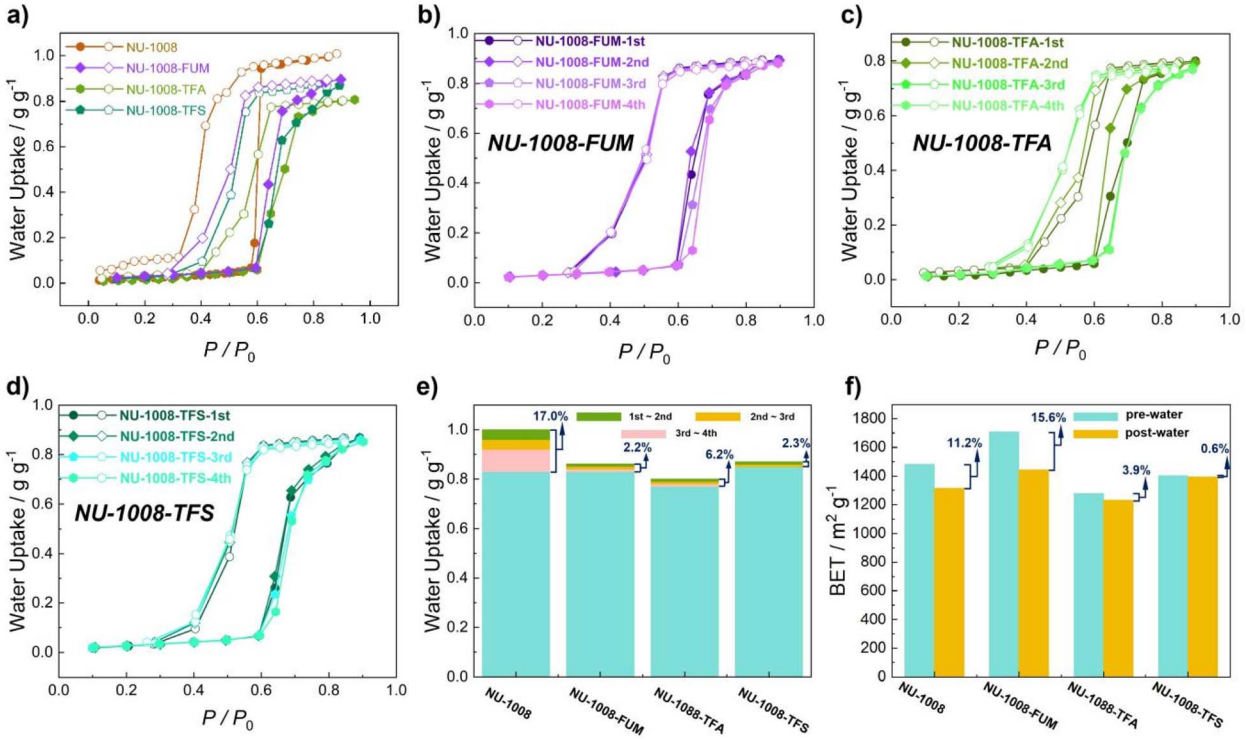

Fig. 3 (a) Water vapor adsorption isotherms measured at 298 K for NU-1008 analogues; (b–d) cyclic water vapor adsorption–desorption isotherms demonstrating the stability of NU-1008-TFA (b), NU-1008-FUM (c), and NU-1008-TFS (d); (e) evolution of the saturated water uptake capacity over multiple cycles; (f) comparison of BET surface areas derived from N_2 adsorption isotherms before and after the cycling tests.

of 2.2% over four cycles (Fig. 3b and e). NU-1008-TFS combines the advantages of both modification strategies: it retains high fluorine content for hydrophobicity around the Zr_6 nodes, while the tetrafluorsuccinate (TFS) anions also bridge neighboring Zr_6 clusters within the *c*-pore. Consequently, NU-1008-TFS delivered performance comparable to NU-1008-FUM, exhibiting a low capacity loss of 2.3% after four cycles.

Both FUM and TFS ligands enable the materials to retain high water uptake capacity over multiple cycles, demonstrating that bitopic linkers provide superior structural reinforcement compared to monotopic ligands in mitigating framework stress from capillary forces. To further assess structural integrity of both samples, N_2 adsorption isotherms at 77 K were collected for each sample after the cycling stability tests and compared with the pre-cycling data (Fig. S9, S15, S21 & S26). As summarized in Table 1, the post-cycling BET surface areas for NU-1008, NU-1008-TFA, NU-1008-FUM, and NU-1008-TFS are 1315.6, 1230.0, 1442.5, and 1392.2 $m^2\ g^{-1}$, respectively. Compared to their initial values prior to water-vapor exposure, these represent declines of 11.2%, 3.9%, 15.6%, and 0.6%, respectively (Fig. 3f and Table 1). The pronounced reduction in the BET surface area of NU-1008-FUM may be attributed to a contraction in the *c*-pore distance along the *c*-axis, likely induced by a conformational adaptation of the FUM linker under repetitive capillary stress. Among all analogues, NU-1008-TFS exhibits the most exceptional cycling stability with minimal structural degradation.

Water adsorption kinetics

Building upon NU-1008-TFS, we further investigated the influence of crystal dimensions on water adsorption kinetics. By modulating solvothermal reaction conditions, a series of NU-1008 crystals with controlled dimensions were successfully synthesized, ranging from acorn-shaped particles (denoted as NU-1008-O) to short-rod (NU-1008-I) and long-rod morphologies (NU-1008-II), and finally to a bulk single crystal (NU-1008-SC). Subsequent functionalization of their *c*-pores with TFS yielded the corresponding analogues: NU-1008-O-TFS, NU-1008-I-TFS, NU-1008-II-TFS, and NU-1008-SC-TFS. NU-1008-O-TFS exhibits an acorn-like morphology with a uniform particle diameter of approximately 1 μm. The short-rod analogue NU-1008-I-TFS possesses a similar cross-sectional size (~1.5 μm), but its length along the mesopore direction extends to about 6 μm, indicating pronounced anisotropic growth along the *c*-axis. In contrast, NU-1008-II-TFS displays a long-rod morphology with a cross-section of 8–10 μm and a length exceeding 80 μm. This dimensional anisotropy is reflected in the length-to-diameter ratios, which are approximately 1, 4–5, and 10 for NU-1008-O-TFS, NU-1008-I-TFS, and NU-1008-II-TFS, respectively.

Water adsorption kinetic studies revealed a correlation between the adsorption rate and particle morphology. Saturation times decreased progressively with the increasing aspect ratio: NU-1008-O-TFS required ~300 min to reach saturation, NU-1008-I-TFS ~200 min, and NU-1008-II-TFS ~150 min. This trend appears counterintuitive to classical diffusion models,

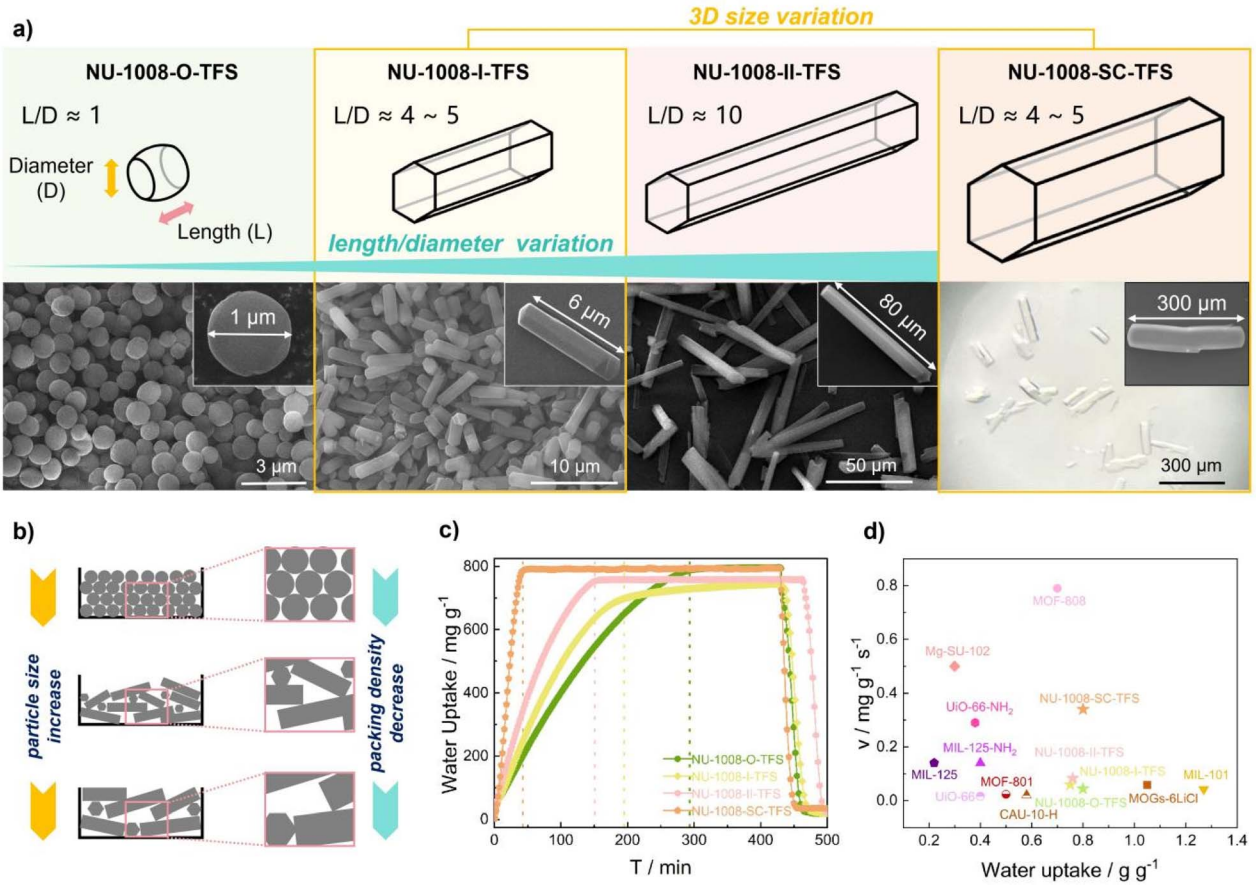

Fig. 4 (a) Schematic illustrations and corresponding SEM/optical images of acorn-shaped NU-1008-O-TFS, short-rod-shaped NU-1008-I-TFS, long-rod-shaped NU-1008-II-TFS, and single-crystal NU-1008-SC-TFS, showing their progressive increase in the length-to-diameter ratio and overall three-dimensional size; (b) schematic representation of the correlation between the particle size and packing density in powder samples; (c) comparative analysis of the water-vapor adsorption kinetics for NU-1008-O-TFS, NU-1008-I-TFS, NU-1008-II-TFS, and NU-1008-SC-TFS; (d) plot comparing the water adsorption rate and capacity of various MOF materials.

since TFS functionalization seals the side windows (*c*-pores), confining water vapor diffusion strictly to the one-dimensional channels along the *c*-axis. Under such conditions, longer particles would be expected to exhibit slower diffusion and thus longer saturation times. A direct comparison between NU-1008-I-TFS and the bulk single-crystal NU-1008-SC-TFS—which share similar aspect ratios ($L/D \approx 4$–5)—highlights this discrepancy: NU-1008-SC-TFS achieves saturation in only ~50 min, compared to ~200 min for NU-1008-I-TFS. This result indicates that the aspect ratio alone does not govern adsorption kinetics. Instead, the overall three-dimensional crystal size plays a more decisive role. Notably, as the crystal size increases from the smallest (NU-1008-O-TFS) to the largest (NU-1008-SC-TFS), the packing density of the powder samples decreases (Fig. 4b). The resultant larger interparticle voids in samples composed of bulk crystals facilitate faster vapor diffusion throughout the bed, thereby accelerating the overall adsorption kinetics.

For indoor humidity control applications, rapid response to humidity variations and high moisture uptake capacity are key requirements for an effective smart adsorbent material. We have compiled comparative data on water uptake capacity and adsorption rates for several prominent MOF materials,[50–54] as summarized in Fig. 4d and Table S2. The analysis shows that Mg-Su-102, although not aiming at indoor humidity control, exhibits the most favorable water adsorption kinetics (0.5 mg g^{-1} s^{-1}), yet its uptake capacity remains limited (0.3 g g^{-1}).[55] MIL-101(Cr) demonstrates the highest water uptake capacity (1.27 g g^{-1}), while its adsorption kinetics are comparatively slow (0.042 mg g^{-1} s^{-1}).[53] Although MOF-808 shows a high water uptake capacity (0.70 g g^{-1}) and very rapid adsorption kinetics (0.79 mg g^{-1} s^{-1}) at 70 RH%,[54] it in its un-functionalized form is limited by its poor water-vapor cycling stability.[11] In contrast, NU-1008-SC-TFS achieves both a high water uptake capacity (0.80 g g^{-1}) and favorable adsorption kinetics (0.34 mg g^{-1} s^{-1}), positioning it as an excellent candidate for smart indoor humidity regulation.

Conclusions

In summary, this work addresses the cycling stability challenge in Zr-MOFs for humidity control by employing the Solvent Assisted Ligand Incorporation (SALI) method. Functionalization of the *c*-pore area within NU-1008 with various auxiliary ligands successfully restricted pore accessibility along the one-

dimensional channel direction. Among these, the bidirectional coordinating tetrafluorosuccinic acid (TFS) proved the most effective, yielding NU-1008-TFS with exceptional stability. This modified material retained 97.7% of its initial water uptake capacity after four adsorption–desorption cycles, and its BET surface area remained at 99.4% of the pre-cycled value, demonstrating robust structural integrity. Investigation into adsorption kinetics revealed a key correlation with particle-size-induced packing density rather than particle morphology. The ultimate bulk single-crystal derivative, NU-1008-SC-TFS, successfully integrates this enhanced stability with a high equilibrium water vapor uptake and rapid adsorption kinetics, establishing it as a highly promising candidate for energy-efficient adsorption-based intelligent humidity regulation.

This study not only resolves the anomaly identified in our prior structural design rules for stable Zr-MOFs but also reaffirms the critical importance of restricting water accessibility to Zr_6 clusters along one-dimensional channels for achieving exceptional cycling stability. Based on this, the present study integrates the site-specific functionalization SALI strategy with the original geometric design principles, establishing a new more adaptable paradigm for designing Zr-MOF water vapor adsorption materials. This paradigm not only upholds the core concept of utilizing one-dimensional channels and limited cluster spacing (<5.4 Å) to construct intrinsic stability, but also further achieves precise chemical modification and reinforcement of specific hydrolysis-prone sites (such as *c*-pore formate ligands) through the SALI method. This dual strategy of "geometric constraint" and "chemical reinforcement" effectively addresses the limitations that may arise from relying solely on structural parameters, significantly enhancing the robustness of the materials under practical cyclic operating conditions. Therefore, this integrated approach provides a more universal and reliable pathway for the future rational design and development of water vapor adsorption MOF materials that combine high capacity, fast kinetics, and ultra-long cycle life.

Author contributions

Hao Lin: writing – original draft, investigation, data curation, formal analysis, validation, methodology. Huiying Lin: data curation, investigation, validation, formal analysis, visualization. Mingxing Zhang: formal analysis, visualization. Yingpeng Jiang: validation, formal analysis, visualization. Yuhang Liu: investigation, visualization. Liting Du: writing – review & editing, methodology, validation. Zhiyong Lu: conceptualization, funding acquisition, writing – review & editing, resources, supervision, visualization.

Conflicts of interest

There are no conflicts to declare.

Data availability

CCDC 2513590 and 2501574–2501576 contain the supplementary crystallographic data for this paper.[56a–d]

All data generated or analyzed during this study are included in this published article and its supplementary information (SI). Supplementary information: ^{1}H NMR and ^{19}F NMR spectra of MOF materials, crystallographic data, PXRD patterns and SEM images. See DOI: https://doi.org/10.1039/d5sc10222g.

Acknowledgements

We are thankful for the financial support from the National Natural Science Foundation of China (22573048). Y.J. gratefully acknowledges support from the Postgraduate Research & Practice Innovation Program of Jiangsu Province (SJCX25_0580).

References

1 P. Lucero-Gómez, E. Balliana, F. C. Izzo and E. Zendri, *Build. Environ.*, 2020, **185**, 107147.
2 X. Xu, Z. Zhong, S. Deng and X. Zhang, *Energy Build.*, 2018, **162**, 163.
3 R. E. Davis, G. R. McGregor and K. B. Enfield, *Environ. Res.*, 2016, **144**, 106.
4 P. Wolkoff, *Int. J. Hyg Environ. Health*, 2018, **221**, 376.
5 P. Wolkoff, K. Azuma and P. Carrer, *Int. J. Hyg Environ. Health*, 2021, **233**, 113709.
6 L. Liu, S. Tan, T. Horikawa, D. D. Do, D. Nicholson and J. Liu, *Adv. Colloid Interface Sci.*, 2017, **250**, 64.
7 W. Shi, W. Guan, C. Lei and G. Yu, *Angew. Chem., Int. Ed.*, 2022, **61**, e202211267.
8 M. Wang, E. Liu, T. Jin, S.-u. Zafar, X. Mei, M.-L. Fauconnier and C. De Clerck, *Water Res.*, 2024, **250**, 121052.
9 N.-X. Zhu, Z.-W. Wei, C.-X. Chen, X.-H. Xiong, Y.-Y. Xiong, Z. Zeng, W. Wang, J.-J. Jiang, Y.-N. Fan and C.-Y. Su, *Angew. Chem., Int. Ed.*, 2022, **61**, e202112097.
10 J. Liu, R. Anderson, K. M. Schmalbach, T. R. Sheridan, Z. Wang, N. M. Schweitzer, A. Stein, N. A. Mara, D. Gomez-Gualdron and J. T. Hupp, *J. Mater. Chem. A*, 2022, **10**, 17307.
11 Z. Lu, J. Duan, L. Du, Q. Liu, N. M. Schweitzer and J. T. Hupp, *J. Mater. Chem. A*, 2022, **10**, 6442.
12 Y. Chen, H. Xie, Y. Zhong, F. Sha, K. O. Kirlikovali, X. Wang, C. Zhang, Z. Li and O. K. Farha, *J. Am. Chem. Soc.*, 2024, **146**, 11202.
13 H. Furukawa, F. Gándara, Y.-B. Zhang, J. Jiang, W. L. Queen, M. R. Hudson and O. M. Yaghi, *J. Am. Chem. Soc.*, 2014, **136**, 4369.
14 W. Gong, Y. Geng, P. Gao, J. Zhang, K. Zhou, J. Dong, O. K. Farha and Y. Cui, *J. Am. Chem. Soc.*, 2024, **146**, 21806.
15 W. Gong, H. Xie, K. B. Idrees, F. A. Son, Z. Chen, F. Sha, Y. Liu, Y. Cui and O. K. Farha, *J. Am. Chem. Soc.*, 2022, **144**, 1826.
16 S.-M. Shih and L.-C. Lin, *J. Am. Chem. Soc.*, 2025, **147**, 34791.
17 Z. Zheng, N. Hanikel, H. Lyu and O. M. Yaghi, *J. Am. Chem. Soc.*, 2022, **144**, 22669.
18 J. Lee, D. Park, E. Jin, S. Lee, J. Lee, H. Oh and W. Choe, *Adv. Funct. Mater.*, 2025, **35**, 2413200.
19 H. An, Y. Chen, Y. Wang, X. Liu, Y. Ren, Z. Kang, J. Li and L. Li, *Chem. Eng. J.*, 2023, **461**, 141955.

20 M. A. van der Veen, S. Canossa, M. Wahiduzzaman, G. Nenert, D. Frohlich, D. Rega, H. Reinsch, L. Shupletsov, K. Markey, D. E. De Vos, M. Bonn, N. Stock, G. Maurin and E. H. G. Backus, *Adv. Mater.*, 2024, **36**, 2210050.
21 J. Hastings, T. Lassitter, Z. Zheng, S. Chheda, J. I. Siepmann, L. Gagliardi, O. M. Yaghi and T. G. Glover, *J. Phys. Chem. C*, 2024, **128**, 11328.
22 Y. Geng, Y. Gao, P. Gao, J. Zhang, X. Tang, J. Dong, J. Jiao, H. Niu, W. Gong and Y. Cui, *J. Am. Chem. Soc.*, 2025, **147**, 7663.
23 A. J. Rieth, A. M. Wright, G. Skorupskii, J. L. Mancuso, C. H. Hendon and M. Dincă, *J. Am. Chem. Soc.*, 2019, **141**, 13858.
24 J. Pang, W. Jiang, X.-W. Zhang, H.-L. Zhou, Y. Sun, W. Gong, B. Wang, F. Ma, L. He, L. Chen, Q. Chen, H.-Q. Zheng, Y. Cui, W.-J. Shi, C. Zhang, M. Wang, Y.-B. Zhang, J.-P. Zhang, C. Zhong, Y. Cui, S. Wang, J.-R. Li, G. Qian, T.-B. Lu, H. Pang and X.-H. Bu, *Sci. China Chem.*, 2025, **68**, 1642–1702.
25 J. Xiao, Z. Zhu, Y. Huang, R. Li and S. Yuan, *ACS Appl. Mater. Interfaces*, 2026, **18**, 5180–5193.
26 M. Li, C. Li, Y. Shi, H. Zhang, Z. Fan, Y. Liu, J. Zhang, J. Pang and X.-H. Bu, *Angew. Chem., Int. Ed.*, 2025, **64**, e202510810.
27 H. Zhang, Y. Shi, T. Chen, Z. Fan, T. Zhang, P. Dong, M. Li, F. Lang, K. Yang, J. Pang and X.-H. Bu, *Angew. Chem., Int. Ed.*, 2026, **65**, e23106.
28 Z. Zhu, J. Xiao, M. Zhang, Y. Huang and S. Yuan, *Chem. Sci.*, 2025, **16**, 22638–22646.
29 J. Xiao, J. Ma, Z. Zhu, Y. Huang and S. Yuan, *J. Mater. Chem. A*, 2025, **13**, 26431–26440.
30 C. Li, J. Zhang, Y. Lian, K. Zhang, H. Zhang, L. Xu, Y. Liu, F. Lang, J. Pang and X.-H. Bu, *Natl. Sci. Rev.*, 2025, **12**, nwaf326.
31 C. Li, H. Zhang, F. Lang, Y. Liu, L. Xu, X.-J. Xi, Y. Li, J. Pang, H.-C. Zhou and X.-H. Bu, *Nat. Commun.*, 2025, **16**, 1405.
32 J. Pang, Z. Zhang, S. Zhang, X. Guo, Q. Chen, X.-W. Zhang, H.-L. Zhou, W. Gong, S. S. A. Shah, C. Zhong, J.-R. Li, J.-P. Zhang, Y. Cui, H.-L. Jiang and X.-H. Bu, *Sci. China Chem.*, 2025, **68**, 1230–1286.
33 C. A. Fernandez, S. K. Nune, H. V. Annapureddy, L. X. Dang, B. P. McGrail, F. Zheng, E. Polikarpov, D. L. King, C. Freeman and K. P. Brooks, *Dalton Trans.*, 2015, **44**, 13490.
34 R. G. AbdulHalim, P. M. Bhatt, Y. Belmabkhout, A. Shkurenko, K. Adil, L. J. Barbour and M. Eddaoudi, *J. Am. Chem. Soc.*, 2017, **139**, 10715.
35 L. Shi, K. O. Kirlikovali, Z. Chen and O. K. Farha, *Chem*, 2024, **10**, 484.
36 M. Ejeian and R. Z. Wang, *Joule*, 2021, **5**, 1678.
37 M. Panahi-Sarmad, T. Guo, S. A. Hashemi, A. Ghaffarkhah, S. Wuttke, M. Arjmand, O. J. Rojas and F. Jiang, *Adv. Mater.*, 2026, **38**, 2413353.
38 X. Liu, X. Wang and F. Kapteijn, *Chem. Rev.*, 2020, **120**, 8303.
39 M. J. Kalmutzki, C. S. Diercks and O. M. Yaghi, *Adv. Mater.*, 2018, **30**, 1704304.
40 L. Cheng, Y. Dang, Y. Wang and K.-J. Chen, *Mater. Chem. Front.*, 2024, **8**, 1171.
41 Z. Lu, H. Lin, Y. Jiang, B. Wei, L. Du, Z. Tong, H. Tan, Y. Liu and J. Bai, *Angew. Chem., Int. Ed.*, 2025, **64**, e202512722.
42 Z. Lu, J. Duan, H. Tan, L. Du, X. Zhao, R. Wang, S. Kato, S. Yang and J. T. Hupp, *J. Am. Chem. Soc.*, 2023, **145**, 4150.
43 A. W. Peters, K. Otake, A. E. Platero-Prats, Z. Li, M. R. DeStefano, K. W. Chapman, O. K. Farha and J. T. Hupp, *ACS Appl. Mater. Interfaces*, 2018, **10**, 15073.
44 Z. Lu, H. Tan, H. Lin, X. Cai, L. Du and Q. Liu, *Chem. Mater.*, 2024, **36**, 2652.
45 F. Lang, L. Zhang, Y. Li, X.-J. Xi, J. Pang, W. Zheng, H.-C. Zhou and X.-H. Bu, *Angew. Chem., Int. Ed.*, 2025, **64**, e202422517.
46 J. Lyu, X. Zhang, K.-i. Otake, X. Wang, P. Li, Z. Li, Z. Chen, Y. Zhang, M. C. Wasson, Y. Yang, P. Bai, X. Guo, T. Islamoglu and O. K. Farha, *Chem. Sci.*, 2019, **10**, 1186.
47 M. R. Popović-Nikolić, G. V. Popović, K. Stojilković, M. Dobrosavljević and D. D. Agbaba, *J. Chem. Eng. Data*, 2018, **63**, 3150.
48 W. Gong, H. Xie, K. H. Cho, X. Tang, J. Park, Z. Chen, J. Dong, O. K. Farha and Y. Cui, *J. Am. Chem. Soc.*, 2025, **147**, 1214.
49 Y. Jiang, H. Tan, B. Wei, L. Du, J. Zhang and Z. Lu, *J. Mater. Chem. A*, 2025, **13**, 31469.
50 X. Zhou, G. Ma, W. Li, M. Cao, L. Nie, N. Han, J. Li, J. Gao, C. Yang and Y. Chen, *Adv. Funct. Mater.*, 2025, e26552.
51 B. Han, M. S. Ng and A. Chakraborty, *Chem. Eng. J.*, 2025, **521**, 166607.
52 C. Çamur, R. Babu, J. A. Suárez del Pino, N. Rampal, J. Pérez-Carvajal, P. Hügenell, S.-J. Ernst, J. Silvestre-Albero, I. Imaz, D. G. Madden, D. Maspoch and D. Fairen-Jimenez, *Adv. Mater.*, 2023, **35**, 2209104.
53 C. Ma, J. Li, G. Wang, Z. Li, W. Su and Y. Zhou, *Nano Lett.*, 2025, **25**, 5778.
54 M. W. Logan, S. Langevin and Z. Xia, *Sci. Rep.*, 2020, **10**, 1492.
55 J. Oppenheim, Z. Yang, B. Dinakar and M. Dincă, *Nat. Commun.*, 2025, **16**, 4297.
56 (*a*) CCDC 2513590: Experimental Crystal Structure Determination, 2026, DOI: 10.5517/ccdc.csd.cc2qclk8; (*b*) CCDC 2501574: Experimental Crystal Structure Determination, 2026, DOI: 10.5517/ccdc.csd.cc2pz2yq; (*c*) CCDC 2501575: Experimental Crystal Structure Determination, 2026, DOI: 10.5517/ccdc.csd.cc2pz2zr; (*d*) CCDC 2501576: Experimental Crystal Structure Determination, 2026, DOI: 10.5517/ccdc.csd.cc2pz30t.